Journal of Nuclear Materials 510 (2018) 1–9

Contents lists available at ScienceDirect

Journal of Nuclear Materials

journal homepage: www.elsevier.com/locate/jnucmat

Radiation tolerance of nickel–graphene nanocomposite with disordered graphene

Hai Huang [a], Xiaobin Tang [a, b, *], Feida Chen [a], Jian Liu [a], Xiangyu Sun [a], Lulu Ji [a]

[a] Department of Nuclear Science & Engineering, Nanjing University of Aeronautics and Astronautics, Nanjing, 210016, China
[b] Jiangsu Key Laboratory of Nuclear Energy Equipment Materials Engineering, Nanjing, 210016, China

HIGHLIGHTS

- Metal–graphene interfaces are expected to heal radiation-induced defects.
- Whether disordered graphene can affect the radiation tolerance is still unclear.
- Graphene would be continuously disrupted by elevated temperatures and irradiation.
- Lesser crystal defects and smaller helium bubbles are observed in the composites.
- Excellent radiation tolerance can be also attributed to graphene's own capability.

GRAPHICAL ABSTRACT

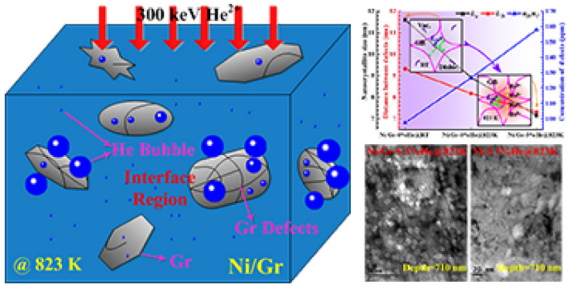

ARTICLE INFO

Article history:
Received 9 March 2018
Received in revised form
24 July 2018
Accepted 25 July 2018
Available online 26 July 2018

Keywords:
Nickel–graphene nanocomposite
Interfaces
Disordered graphene
Helium-ion irradiation
Radiation tolerance

ABSTRACT

Metal–graphene nanocomposites are expected to have excellent radiation tolerance, and may become a candidate structural material for advanced fission reactors. Nevertheless, whether the structural disorder of graphene introduced by preparation or irradiation can strongly affect the radiation tolerance of the composites is still unclear. Here we investigate the radiation tolerance of nickel–graphene nanocomposite by using 300 keV helium-ion irradiation at 823 K. Results showed that the intrinsic crystalline structure of graphene would be continuously disrupted by the elevated temperature and irradiation. However, lesser crystal defects, such as lattice swelling and stacking faults, and smaller helium bubbles are observed in the composite than those in its pure counterpart. The reason may be attributed to graphene's own capability in maintaining two-dimensional structure and inhibiting the formation of large-size defects. Thus, nickel–graphene interfaces can be maintained and their role in healing radiation-induced defects is still able to play. Results of the study highlight the potential of metal–graphene nanocomposites for use as radiation tolerance materials.

1. Introduction

Graphene (Gr) is characterized by high Young's modulus (~1 TPa), high intrinsic strength (~130 GPa), large surface area (~2600 m^2/g), and low density (2.2 g/cm^3) [1]. The two-dimensional nanomaterial exhibits potential as a reinforcing

* Corresponding author. Department of Nuclear Science & Engineering, Nanjing University of Aeronautics and Astronautics, Nanjing, 210016, China.
E-mail address: tangxiaobin@nuaa.edu.cn (X. Tang).

https://doi.org/10.1016/j.jnucmat.2018.07.051
0022-3115/

component to be incorporated and dispersed in metal matrices. This disposal should create a plentiful of ultra-high-strength metal–Gr interfaces and confer pure metals with novel functions [2–5]. Excellent radiation tolerance may be one of the most outstanding features of metal–Gr nanocomposites. It has long been known that grain boundaries (GBs) and hetero-interfaces can serve as sinks for radiation-induced defects and traps for helium (produced as a transmutation product under neutron irradiation) [6–13]. Similarly, the high-density metal–Gr interfaces may improve the "self-healing" ability of irradiated defects for the composites. Many research groups have preliminarily explored the radiation tolerance of the composites [14–18]. For example, Yang et al. [14] by *ab initio* calculations demonstrated that the copper–Gr interface provides a strong sink for trapping defects and gives rise to preferential sites for their recombination. Kim et al. [16] performed helium (He) ion irradiation experiments on vanadium–Gr nanocomposite; the resulting composite exhibits higher radiation tolerance than that of its pure counterpart. Si et al. [17] found that a smaller-period-thickness tungsten–Gr nanocomposite exhibits high radiation tolerance in the reduction of He bubble density.

Recent activities to develop advanced fission reactors with better functionality and capability represent an even greater demand on the radiation tolerance of structural materials [19–23]. The materials need to face higher neutron doses at elevated temperatures for long periods of time [24,25]. A large amount of He atoms from (n, α) transmutation reactions are introduced into the materials and trapped in radiation-induced vacancies to form He–vacancy clusters at an elevated temperature [26–30]. The process may ultimately result in swelling, blistering of metal surfaces, and embrittlement, thereby deteriorating the structural integrity of materials and reducing the service time of nuclear reactors [27,28,30,31]. Moreover, conventional materials rarely withstand the extreme environment conditions. Therefore, new design concepts for materials that can resist damage under extreme irradiation are urgently needed [12,19,22]. Because of the excellent performance of metal–Gr interfaces on reducing radiation-induced defects and preventing He atoms agglomerating to coarse bubbles, metal–Gr nanocomposites can provide a path for the goal. Nevertheless, previous studies on radiation damage rarely include the surface morphology of Gr and its effect on the radiation tolerance of the composites. Owing to the pivotal role of Gr in forming metal–Gr interfaces, the structural disorder of Gr may pose a major challenge to the potential application of the composites as radiation-tolerant materials.

The Gr component of metal–Gr nanocomposites is mainly obtained via two methods, namely, chemical vapor deposition [2,16,17,32] and reduction from Gr oxide (GO) by means of chemical and thermal reaction [33,34]. Given the low cost and easily large-scale production [33], reduced GO (RGO) has been more wildly used in the composites [35,36] and can facilitate the mass applications of the composites [36]. However, several works [1,33,37–40] have reported that high-density topological defects and structural disorder, such as vacancies, dislocations, GBs, and holes, can be introduced into RGO via GO reduction [37–39] and composite preparation [1,40]. Moreover, similar topological defects and structural disorder have also been observed in Gr after ion irradiation [41–45]. In our previous simulation work, an interesting phenomenon of copper–Gr nanocomposite was also found [46]: stacking fault tetrahedra are easily induced after relaxation when the size of the intrinsic defect of Gr exceeds a certain threshold (~5 nm). Thus, it is doubtful whether the sink role of metal–Gr interfaces is still present when the Gr is not intact. And what's worse is that neutron irradiation and elevated temperatures in the reactors can synergistically act on the composites, thereby causing a more complicated Gr surface morphology. Thus, some questions need to be answered. For example, can metal–Gr interfaces continue to exist given the above-mentioned conditions? How will the crystal texture of Gr and its metal matrices evolve?

In this work, nickel–Gr (Ni/Gr) nanocomposite was used to investigate radiation tolerance caused by a disordered Gr at 823 K. Pure Ni was used as reference material. Electrodeposition was adopted to synthesize the composite and can create a plentiful of Ni/Gr interfaces. Ni was selected as the matrix because of its potential applications in advanced fission reactors [21] (*e.g.,* molten salt reactor [47] and supercritical water-cooled reactor [48]). Displacement damage and He atoms were introduced by using 300 keV He^{2+} irradiation at 823 K, which can simulate the effects of neutron irradiation on the composite [17,47,49]. The paper is organized as follows. First, the specimens were divided into three groups. Each group adopted a specific approach for post-processing: the first group with prolonged annealing and He-ion implantation at 823 K; the second group with prolonged annealing but no irradiation at 823 K; and the third group with neither annealing nor irradiation at room temperature (RT). The purpose of this treatment is to gradually introduce structural disorder into Gr by thermal reduction and irradiation at an elevated temperature. Then, the microstructure characterizations of the three groups were performed by Raman spectroscopy, grazing incidence X-ray diffraction (GIXRD), and transmission electron microscopy (TEM). Our results show that the disordered morphology of Gr does not hamper the sink role of Ni/Gr interfaces and that the composite continuously realizes excellent radiation tolerance.

2. Methods

2.1. Material and sample preparation

The Ni/Gr was synthesized by electroplating, and the components of the plating solution are shown in Table S1. The GO was prepared by the modified Hummers method [1,37–39,50], and the morphology of GO is shown in Fig. S1. The carbon material was used in the present work as it is easy to disperse as uniform electrolytes, thereby avoiding agglomeration in the composites [40,51]. The size (1–2 μm) and thickness (approximately 0.9 nm) of the GO, as shown in Fig. S2, represent the typical monolayer of GO [1,51]. The pH of the solution was adjusted to 4.0 by sulfuric acid. Plating solution was stirred by magnetic stirring, which could propel GO and Ni ions onto the cathode surface and prevent the GO descending [51]. An electrolytic nickel plate (99.99%) was used as the anode and a polished copper foil with 40 mm × 30 mm × 2 mm was employed as the cathode. The plating was performed at 50 °C with the current density of 3 A/dm^2 for 0.5 h. The uniform distribution of GO in the Ni matrix was confirmed by SEM and EDS (Fig. S3). Pure Ni, which was used as the reference material, was electrodeposited in the same condition. For convenience in conducting the experiments, all specimens were cut to 5 mm × 5 mm (surface area) and divided into three groups.

2.2. He^{2+} ions irradiation

Experiments on He-ion implantation were performed on 320 KV multi-discipline research platform at the Institute of Modern Physics, Chinese Academy of Sciences in Lanzhou. The first two groups of specimens were annealed at 823 K in high-vacuum conditions (~10^{-6} Torr) for 30 min, which can help rapidly reduce GO into RGO [52]. Note that both of GO and RGO will be referred to as Gr hereafter for ease of description. Subsequently, the first group of specimens was irradiated normal to the surface with 300 keV He^{2+} ions at 823 K (approximately half of the melting point of the material, ~0.5 T_m), where irradiation-enhanced "vacancy

mechanisms" have been found to dominate "replace mechanisms" [47,48]. Implantation was conducted to a fluence of 1×10^{17} ions/cm^2. Then, the second group was applied the same temperature environment and amount of time but without irradiation. Damage profiles were simulated using Quick Kinchin Pease Mode of Stopping and Range of Ions in Matter (2013) code (SRIM, 2013) [53]. The displacement energy of 40 eV for Ni was adopted from previous studies [22,47,48]. The results are shown in Fig. S4. The calculated penetration depth of the 300 keV He^{2+} ion is approximately 900 nm below surface. The peak damage approaches ~2.4 dpa at the depth of ~650 nm, and the peak He concentration reaches ~5.3 at.% (or 53,000 appm) at the depth of ~710 nm. The three groups were eventually called Ni/Gr−5.3%He@823K, Ni/Gr−0% He@823K, and Ni/Gr−0%He@RT. Similarly, the three groups of pure Ni were named Ni−5.3%He@823K, Ni−0%He@823K, and Ni−0% He@RT.

2.3. Material characterization

The Raman spectra of Ni/Gr were obtained by a Renishaw inVia Raman Microscope (Renishaw Inc., Chicago, IL) with the following specifications: a laser of wavelength of $\lambda_{laser} = 532$ nm, spectral resolution of 1 cm^{-1}, and a 100 × objective lens (numerical aperture, 0.85) by the line-scan method. To analyze the specimen morphology, the Raman lines were fitted to Lorentzian curves [54,55]. The crystalline structure of the irradiated and un-irradiated specimens was identified by GIXRD (D/MAX-2500, Rigaku Inc., Japan) using a radiation of Cu-Kα (wavelength of $\lambda_{Cu\text{-}K\alpha} = 0.15405$ nm) in a wide range of diffraction angles (2θ) from 20° to 90°. TEM (Tecnai G2 20, FEI Company, Holland) with an acceleration voltage of 200 kV was performed to determine the detailed morphology of irradiated samples. The details of TEM analysis and the procedures of cross-sectional TEM sample fabrication are reported in a previous work [13].

2.4. Molecular dynamics

To understand the effects of Ni/Gr interfaces on the behavior of He atoms, a sandwich Ni/Gr model of 2.7 nm × 2.6 nm × 5.3 nm was generated; the details of Gr matching with Ni was presented in our previous study on copper−Gr nanocomposite [15]. All calculations were performed using the classical reactive molecular dynamics (MD) simulations with LAMMPS code [56]. A ReaxFF force field that combines Ni/C/H/noble gas parametrizations was used to describe the atomic interactions [57]. The noble gas interacts with the Ni and C atoms only through van der Waals interactions, which are described in ReaxFF using a Morse potential [18]. The minimum energy configuration was obtained by applying the conjugate gradient algorithm under zero external pressure to release the stress out of the system. In addition, the system was simulated by using periodic boundary conditions along all three axes in consideration of the relatively small number of atoms used in the simulations. Initially, He atoms were randomly inserted to produce the He concentration of ~2 at.%. After insertion, the model was relaxed at 0 K for 10 ps? Subsequently, the temperature was rescaled to desired values (~823 K) and kept constant thereafter. The NVT ensemble (constant number of atoms, volume, and temperature) was employed to keep temperature constant with a timestep of 0.5 fs for 1 ns? The visualizations of the results were rendered with OVITO code [58].

3. Results

3.1. Surface morphology of Gr

The Raman spectra of Gr of Ni/Gr are shown in Fig. 1; the observed peaks are labeled as D and G following the observations reported in other works [34,40,51]. The two peaks are focused because of their close relationship with the structural disorder of Gr [40,54,55,59]. The Raman lines were fitted into the two lines centered near 1350 cm^{-1} for the D band and 1585 cm^{-1} for the G band. The fitting factor (R^2) of ~0.97 or higher was obtained for fits of the data to Lorentzian lines. The intensity ratio (I_D/I_G, corresponding to the peak area ratio [54,59]), positions, and full widths at half-maximum (FWHM or Γ) of D and G peaks of the three groups are also summarized in Fig. 1. To understand the different Raman peak evolutions, the physical mechanism of Raman scattering related to these peaks [55,60] are considered. The G band, which is associated with the doubly degenerate phonon mode (E_{2g} symmetry) at Brillouin zone center, is caused by the bond stretching of all pairs of sp^2 atoms in six-fold aromatic rings and C−C chains. The D band, which originates from the breathing modes of sp^2 atoms in rings, involves a defect-related scattering process. For the rings of Gr, as long as only one bond is broken by irradiation or elevated temperatures, the breathing mode will disappear, while the other bonds continuously contribute to the stretching vibration. Consequently, the evolution of disorder in Gr can be analyzed by the disorder-induced D-band and Raman-allowed G-band.

In Fig. 1(c), an obvious D peak occurs in Ni/Gr−0%He@RT. The I_D/I_G ratio exceeds 1, which is similar to the results of the study by Pavithra et al. [40]; this phenomenon implies that high-density defects and disorder have existed in the Gr before post-processing. In Fig. 1(a) and (b), the FWHMs of D and G peaks of Ni/Gr−5.3%He@823K and Ni/Gr−0%He@823K relative to those of Ni/Gr−0%He@RT appear with higher fluctuations induced by the extreme conditions, especially the Γ_D increasing rapidly. As a result, the overlap of the two peaks is aggravated. Clearly, the I_D/I_G presents an approximately linear increase because of the gradual

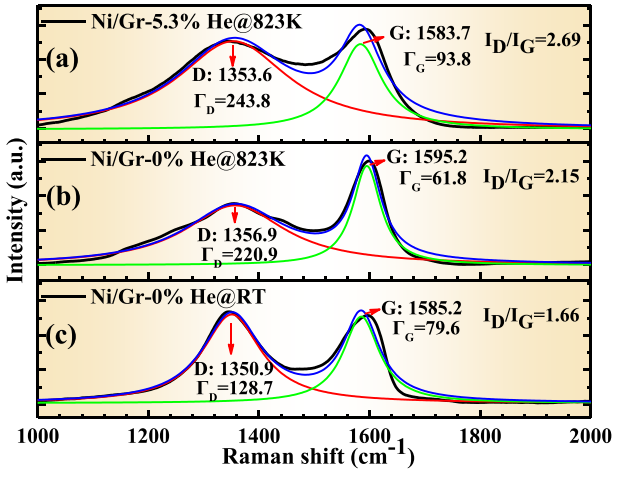

Fig. 1. Raman spectra of three groups of Ni/Gr specimens. Black lines represent the obtained spectra fitted to blue Lorentzian lines with two individual peaks (red and green lines). Peak information (intensity ratio, positions, and FWHM) is also exhibited. (a) Ni/Gr−5.3%He@823K, (b) Ni/Gr−0%He@823K, and (c) Ni/Gr−0%He@RT. (For interpretation of the references to colour in this figure legend, the reader is referred to the Web version of this article.)

introduction of thermal reduction and irradiation at 823 K, which indicates the increase of disorder in Gr. However, no obvious shifts, due to the effects of thermal reduction and irradiation at the elevated temperature, are observed for the two peak positions, suggesting that the Gr is not completely disordered.

3.2. Microstructure of Ni matrix

Fig. 2(a) and (b) show the GIXRD patterns of Ni/Gr and pure Ni, respectively. The diffraction peaks are assigned to (111), (200), and (220) crystalline structures of Ni, and in good agreement with those of the reference patterns for the face-centered cubic Ni (JCPDS data of PDF #04-0850). For comparison, the GIXRD patterns are normalized and the reference pattern of Ni is also exhibited. Evidently, the FWHMs of the diffraction peaks of Ni/Gr–0% He@823K (or Ni–0%He@823K) decrease relative to those of Ni/Gr–0%He@RT (or Ni–0%He@RT), which implies the coarsening of crystalline grains. Nonetheless, the same phenomenon induced by irradiation does not seem to appear. A comparison of the three GIXRD patterns of Ni/Gr or pure Ni shows that the preferred orientation of Ni will be shifted from (111) to (200) or (220) due to the elevated temperature or irradiation. Unlike the recrystallization effect induced by annealing, the irradiation process changes the proportion of specimen orientations by disrupting crystal texture. The proportion of (111) orientation in Ni–5.3%He@823K continuously decreases relative to that of Ni–0%He@823K, while the proportion of (111) orientation in Ni/Gr–5.3%He@823K increases relative to that of Ni/Gr–0%He@RT.

Some information on the Ni lattice structure, such as lattice swelling [61] and stacking faults [62], that is not immediately observable in the shift of diffraction peaks can be extracted from Fig. 2. The effects of elevated temperature and irradiation on the relative change in lattice (*i.e.*, swelling rate $\Delta d = (d - d_0)/d_0$, d_0 for the lattice parameter of the as-deposited specimen) are illustrated in Fig. 3. The d of pure Ni increases with the introduction of elevated temperature and irradiation, while the d of Ni/Gr after annealing or irradiation has almost not change relative to that of as-deposited Ni/Gr. The X-ray diffraction peak-shift method proposed by Warren [63] was used to determine the stacking fault probability (α) of face-centered cubic structure. The equation (in degrees) is as follows [62]:

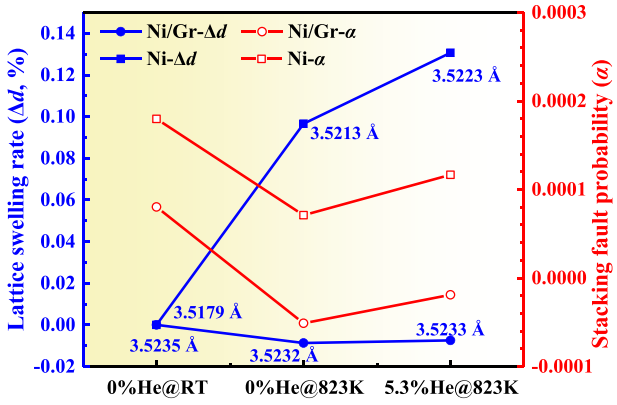

Fig. 3. Lattice swelling rate and stacking fault probability of Ni/Gr and pure Ni after different post-processing. The corresponding lattice parameters of the three groups of specimens (Ni/Gr or pure Ni) are also marked.

$$\Delta(2\theta_{200} - 2\theta_{111}) = \frac{-90\sqrt{3}\,\alpha}{\pi^2}\left[\frac{tan\theta_{200}}{2} + \frac{tan\theta_{111}}{4}\right] \quad (1)$$

where $\Delta 2\theta_{200} = 2\theta_{200} - 2\theta_{200}^{\circ}$ and $\Delta 2\theta_{111} = 2\theta_{111} - 2\theta_{111}^{\circ}$. In the equation, $2\theta_{200}^{\circ}$ and $2\theta_{111}^{\circ}$ represent the peak positions of (111) and (200) planes of the standard specimen without faults. Clearly, the α of Ni/Gr is always less than that of pure Ni, as shown in Fig. 3. The stacking faults of as-deposited Ni matrix can be reduced by annealing. The α of Ni–5.3%He@823K is increased by irradiation. By contrast, the stacking faults of Ni/Gr–5.3%He@823K are not induced by irradiation because the probability value is less than 0, which indicates an impossible event.

The He bubbles of Ni/Gr–5.3%He@823K at different depths (0, 280, 710, and 900 nm) from the surface identified via TEM studies are shown in Fig. 4(a–d). The number density of He bubbles gradually increases as irradiation depth increases. At a depth approaching to that of the peak damage (Fig. 4(c)), a large number of He bubbles occur, and the number density of He bubbles reaches a maximum. Subsequently, He bubbles tend to disappear at the end part of the penetration range. The difference in the number density of He bubbles is very obvious around the end of penetration range, as shown in Fig. 4(d). The He concentration profile of Ni/Gr–5.3%

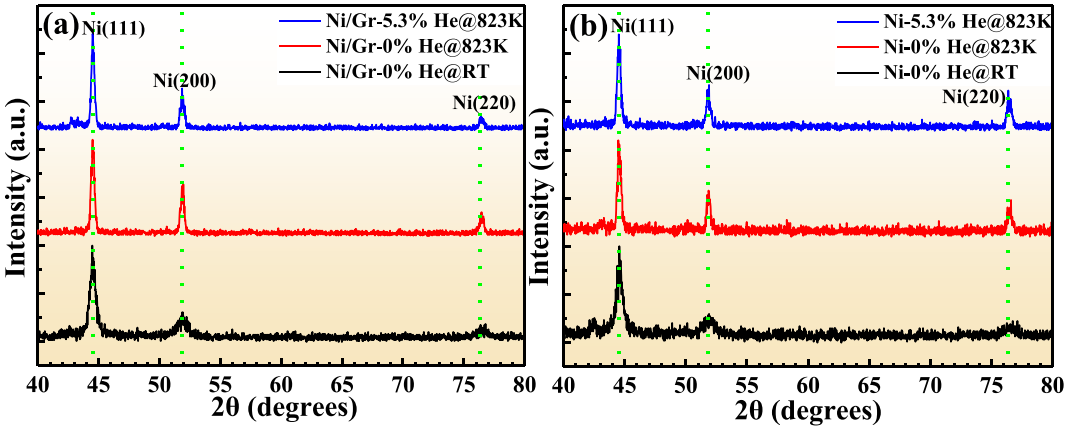

Fig. 2. Normalized GIXRD patterns of Ni matrix. Black lines represent specimens with annealing and irradiation at 823 K; red lines represent specimens with annealing but no irradiation at 823 K; and blue lines represent specimens with neither annealing nor irradiation at RT. The reference patterns of the face-centered cubic Ni are plotted as green dotted lines. The corresponding diffraction peaks are assigned to (111), (200), and (220). (a) Ni/Gr and (b) pure Ni. (For interpretation of the references to colour in this figure legend, the reader is referred to the Web version of this article.)

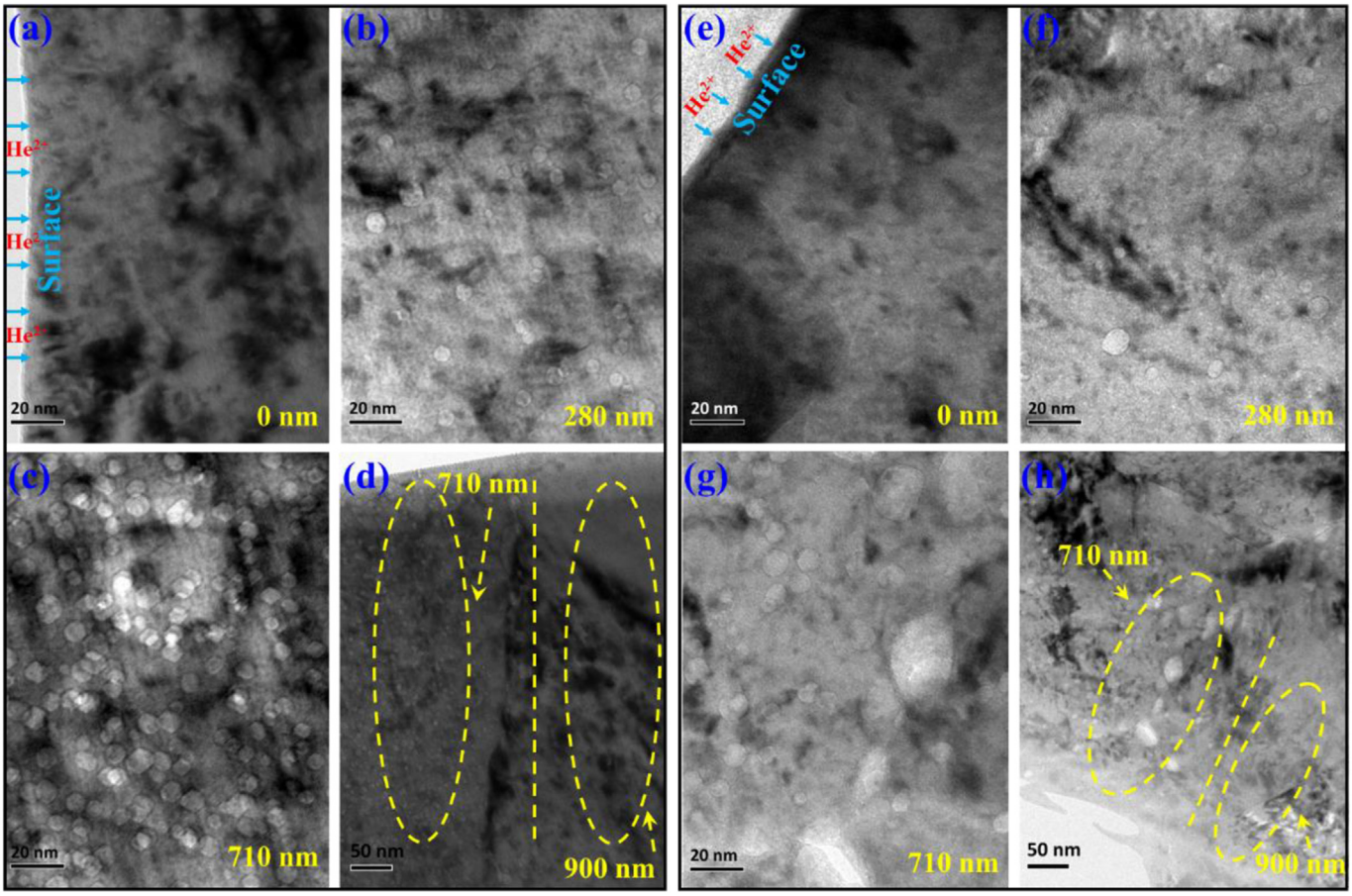

Fig. 4. Irradiation-induced distribution of He bubbles at 823 K. (a–d) Cross-sectional TEM images of Ni/Gr–5.3%He@823K at different depths from surface (0, 280, 710, and 900 nm). (e–h) Cross-sectional TEM images of Ni–5.3%He@823K at different depths from surface (0, 280, 710, and 900 nm). The He bubbles around the end part of the penetration range are highlighted by yellow-dotted ovals for comparison. (For interpretation of the references to colour in this figure legend, the reader is referred to the Web version of this article.)

He@823K is in good agreement with the calculated values using SRIM 2013 (Fig. S4). The variations in He bubble sizes are not obvious at different depths, although the number density changes significantly as a function of implantation depth. A similar distribution of He bubbles also appears in Ni–5.3%He@823K (Fig. 4(e–h) and Fig. S5). However, compared with Ni/Gr–5.3%He@823K, the Ni–5.3%He@823K obtains a smaller number density of He bubbles. In addition, the size of He bubbles of Ni–5.3%He@823K dramatically increases at the region of peak damage. In order to quantify the difference between Ni/Gr–5.3%He@823K and Ni–5.3% He@823K in He bubbles, the size distribution of He bubbles at the region of peak damage is shown in Fig. S6. The average size of He bubbles in Ni/Gr–5.3%He@823K is smaller than that of Ni–5.3% He@823K. This result implies that small He bubbles easily accumulate to form large bubbles in Ni–5.3%He@823K.

4. Discussion

With He-ion irradiation and elevated temperature, the morphology of Gr and its metal matrix is disrupted. However, the Ni/Gr exhibits the better radiation tolerance than the pure Ni, which indicates that the sink role of Ni/Gr interfaces continues to play. The most likely reason should be that the intrinsic crystalline structure of Gr remains largely intact, and no obvious miscibility of Ni atoms around the Gr occurs to eliminate the interfaces.

The surface morphology of Gr in the composite may be speculated by referring to the amorphization trajectory of carbon materials proposed by Ferrari et al. [64]. Crystalline graphite evolves into nanocrystalline (*nc*) graphite (stage I), transforms into a low sp^3 amorphous carbon (*a*-C) (stage II), and eventually forms high sp^3 (tetrahedral) amorphous carbon (*ta*-C) (stage III), as shown in Fig. 5. From the results of Raman spectra in Fig. 1, all Gr components of the three groups can be classified as *nc* because the corresponding I_D/I_G ratios are in the range of 1.66–2.69 whereas the positions of G peaks fluctuate between 1583.7 and 1595.2 cm^{-1}. In addition, owing to the remnant oxygen-containing functional groups with sp^3 phase [33], the Gr of Ni/Gr–0%He@RT is likely in stage II, as shown by the green region of Fig. 5(a). The Gr components of Ni/Gr–0%He@823K and Ni/Gr–5.3%He@823K are also likely in stage II as the elevated temperature or irradiation cannot fully recover sp^2 phase from sp^3 amorphous carbon. The surface morphology of Gr of Ni/Gr–0%He@RT, Ni/Gr–0%He@823K, and Ni/Gr–5.3%He@823K is represented by *A*, *B*, and *C* in Fig. 5, respectively. Clearly, the sp^3 amorphous carbon of Ni/Gr–0%He@823K (*A*) relative to that of Ni/Gr–0%He@RT (*B*) decreases, suggesting that the elevated temperature can reduce Gr by removing oxygen-containing functional groups [33] and repair the disorder of Gr [65]. However, the destruction capability of irradiation toward the Gr seems to be weaker than that of the repair capability of elevated temperature. The proportion of sp^3 amorphous carbon of Ni/Gr–5.3%He@823K (*C*) falls between that of Ni/Gr–0%He@RT (*A*) and Ni/Gr–0%He@823K (*B*). After extreme post-processing, the proportion of sp^3 amorphous carbon of Gr does not exceed the 5% of Gr. On the other hand, the sp^2 defective carbon (*i.e.*, chain or

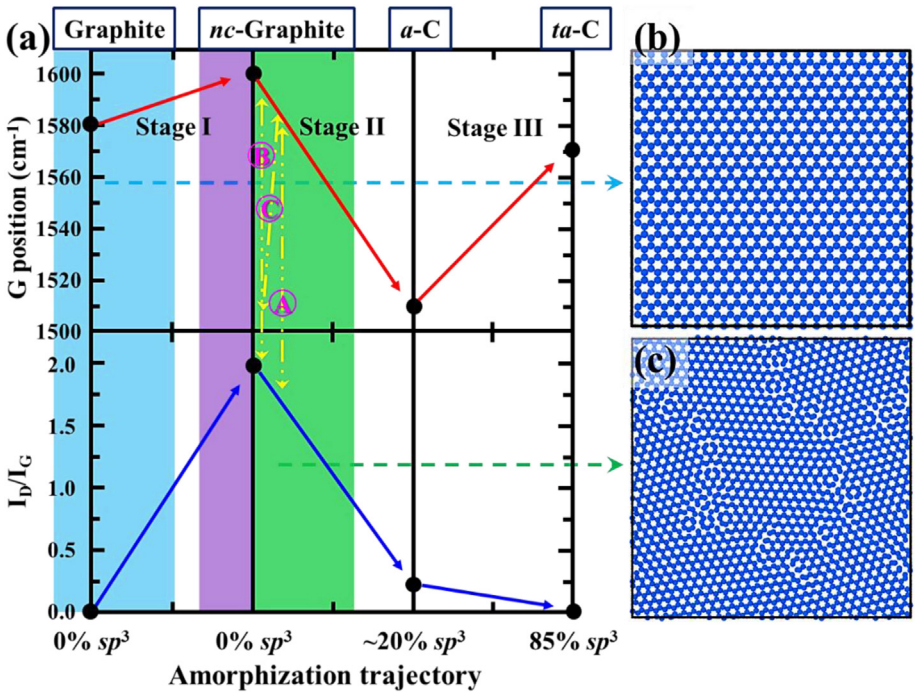

Fig. 5. Amorphization trajectory of carbon materials. (a) A schematic variation of amorphization trajectory versus G position and I_D/I_G ratio [64]. The range of stages I, II, and III of the amorphization trajectory is divided. The graphite state is represented by blue region, while the *nc* graphite state is represented by the violet and green regions. The corresponding surface morphology of the Gr components of Ni/Gr−0%He@RT, Ni/Gr−0%He@823K, and Ni/Gr−5.3%He@823K is marked as *A*, *B*, and *C*, respectively. (b) A hypothetical diagram of the graphite state of Gr. (c) A hypothetical diagram of the *nc* graphite state of Gr. (For interpretation of the references to colour in this figure legend, the reader is referred to the Web version of this article.)

clustering sp^2 phase) may also remain in the Gr components owing to the transition of stage I.

The amount of defects in Gr can be properly quantified using Raman spectroscopy and evaluated for nanocrystallite size (L_a), distance (L_D) between defects, and defect density (n_D) [59,66,67]. All of these parameters are related to the I_D/I_G ratio [66,67]. The general equations for L_a, L_D, and n_D can be written as:

$$L_a(nm) = \left(2.4 \times 10^{-10}\right)\lambda_{laser}^{4}\left(\frac{I_D}{I_G}\right)^{-1} \quad (2)$$

$$L_D(nm) = \sqrt{(1.8 \times 10^{-9})\lambda_{laser}^{4}\left(\frac{I_D}{I_G}\right)^{-1}} \quad (3)$$

$$n_D\left(cm^{-2}\right) = \left(1.8 \times 10^{22}\right)\lambda_{laser}^{-4}\left(\frac{I_D}{I_G}\right) \quad (4)$$

where λ_{laser} represents a wavelength of laser (Methods section). For the honeycomb lattice of a perfect Gr layer, the number of carbon atoms ($n_C = 3.82 \times 10^{15}\ cm^{-2}$) [54] is calculated. The concentration of defects and disorder in parts per million (*ppm*) can be determined by calculating the ratio of n_D/n_C. Therefore, the profile of disordered Gr in Ni/Gr can be accurately delineated using the above-mentioned parameters, the corresponding values of which are shown in Fig. 6. The L_a of the three groups is between 7 and 12 nm, which is consistent with the qualitative perspective. The elevated temperature and irradiation aggravate the transition of Gr from an orderly to disorderly state (*i.e.*, increasing n_D/n_C). The role of elevated temperature also implies that the repair can only achieve sp^3 amorphous carbon to sp^2 defective carbon instead of sixfold aromatic rings. Initially, L_a obtains a higher value than does L_D; subsequently, L_a and L_D are nearly equal. A possible explanation

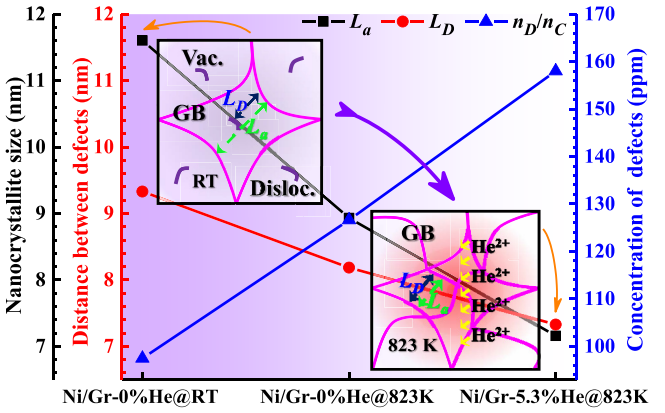

Fig. 6. Quantification of Gr defects. Nanocrystallite size (L_a), distance (L_D) between defects, and defect density (n_D) in the Gr components of Ni/Gr−0%He@RT, Ni/Gr−0% He@823K, and Ni/Gr−5.3%He@823K. The insets correspond to the hypothetical state of Gr in Ni/Gr−0%He@RT and Ni/Gr−5.3%He@823K.

for the phenomena can be given by the insets in Fig. 6. For ease of understanding, L_a is simply regarded as the distance between two disjoint GBs in the same grain, while L_D is the distance between any two defects (*e.g.*, vacancies or dislocations) in the same grain. Normally, L_D is unlikely to be higher than L_a because the defects mainly locate in the grain interior of Gr. At the elevated temperature, the motion of C atoms is accelerated, and the sink role of GBs of Gr is activated. The defects in the grain interior of Gr prefer to migrate toward the GBs of Gr [68]. Meanwhile, the defects at different distance from the GBs of Gr may aggregate and become new sinks before arriving the GBs, thereby resulting in the formation of a mass of new GBs. Due to irradiation, more defects are introduced into the Gr and more new GBs are generated.

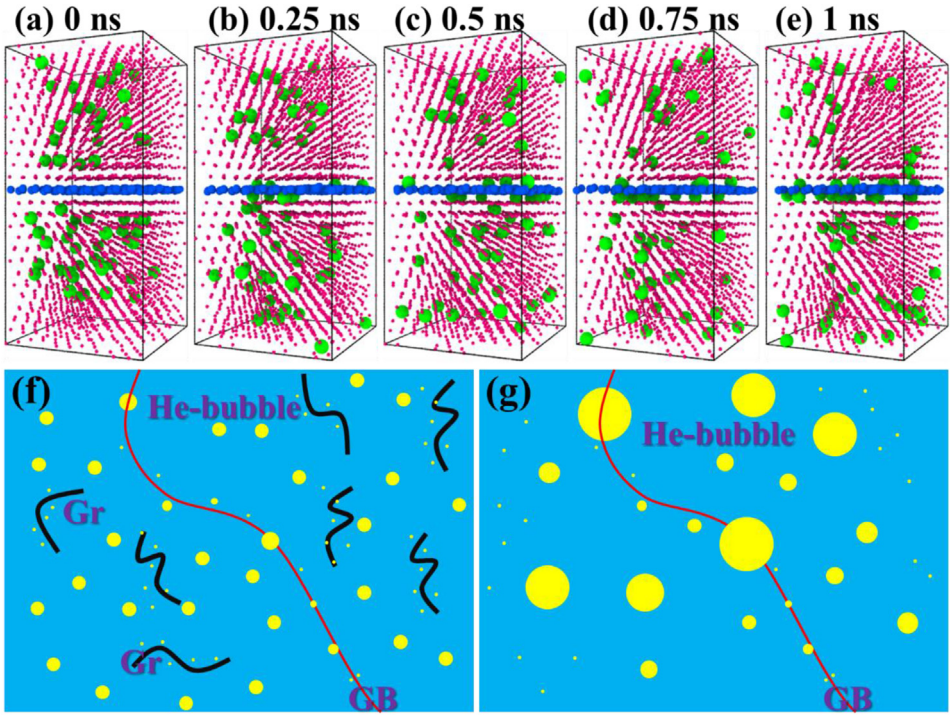

Fig. 7. Migration and clustering of He atoms at 823 K. (a–e) Migration of He atoms near the Ni/Gr interface during 1 ns? Green, pink, and blue spheres represent He, Ni, and C atoms, respectively. ((f) and (g)) Conceptual schematic of the clustering of He atoms in Ni/Gr and pure Ni. He bubbles, Gr, and GB are illustrated by yellow spheres and black and red curves, respectively. (For interpretation of the references to colour in this figure legend, the reader is referred to the Web version of this article.)

Consequently, the original grain of Gr is continuously subdivided, but the two-dimensional structure is still able to maintain.

Our previous simulation studies [46] showed that stacking faults near copper–Gr interfaces during cascade collisions are likely triggered by the Gr defects with the size higher than 2 nm. In view of the higher cohesive energy between Ni and Gr than that between copper and Gr [69], the Ni/Gr under the same conditions as those of copper–Gr nanocomposite can easily form stacking faults near the interfaces during irradiation. The results that the stacking faults of Ni/Gr are removed by annealing and that no additional stacking faults are introduced into the Ni/Gr by irradiation imply that the size of Gr defects in Ni/Gr does not exceed 2 nm and that the Ni/Gr interfaces remain stable after irradiation at the elevated temperature. Thus, the displacement damage and He atoms in the Ni matrix can be reduced by Ni/Gr interfaces. Unlike in pure Ni, lattice swelling does not occur in Ni/Gr. From Fig. 2, the opposite change in the proportion of (111) for Ni/Gr–5.3%He@823K and Ni–5.3% He@823K can also be explained by the Gr and its interfaces. After He-ion irradiation, all of the peak intensities are likely to decrease due to the increase in amorphous metal. The decrease of (111) may be most obvious of all orientations because it possesses the largest proportion and is the most easily damaged. However, owing to the preference of Gr to combine with Ni(111) [2,51,69], radiation damage can be suppressed by the Ni/Gr interfaces, and the proportion of (111) in Ni/Gr–5.3%He@823K are likely to realize fewer reductions as opposed to that in Ni–5.3%He@823K.

The *nc* structure of Gr occupies the widest region in Ni/Gr interfaces. Thus, the sink role of Ni/Gr interfaces may mainly play around each *nc* region of Gr. To explore the capability of Ni/Gr interfaces, an Ni/Gr model with Gr of 2.7 nm × 2.6 nm and ~2 at.% He atoms was used and observed for the evolution of He atoms at 823 K (Fig. 7(a–e)). During relaxation, the He atoms migrated along the crystal channel of Ni and into the Ni/Gr interface. The He atoms adsorbed by the Ni/Gr interface were difficult to return to the matrix and instead randomly moved along the interface. After 1 ns, nearly one-third of the He atoms stayed in the interface and very few He clusters were observed in the matrix (detailed simulations in Supplementary Movie). The strong role of the Ni/Gr interface with *nc* Gr in adsorbing radiation-induced defects may explain the phenomena of Fig. 4, and was vividly illustrated in Fig. 7(f). High levels of radiation-induced displacement damage in the form of vacancies and self-interstitial atoms (SIAs) are generated in the composite by He-ion irradiation. Considering the stability of Ni/Gr interfaces and the crystalline coarsening of Ni matrix at the elevated temperature, the high-density Ni/Gr interfaces exert a greater impact on the defects than do GBs. Owing to the significantly low migration energy [22,70], more SIAs relative to vacancies are preferentially absorbed by the interfaces during diffusion at 823 K. Consequently, the annihilation of vacancies and SIAs obviously decreases, and the surviving vacancies are dispersed due to the high-density Ni/Gr interfaces. These vacancies can trap He atoms to form He–vacancy complexes, which can act as nucleation points for He bubble formation, thereby resulting in the high number density of He bubbles. On the other hand, as shown in Fig. 7(a–e), a lot of He atoms are also absorbed by the interfaces. Subsequently, the He concentration of Ni matrix can decrease, thereby restraining the growth of He bubbles. However, in pure Ni, owing to the lack of interfaces and the high He concentration, the He–vacancy complexes can easily trap other vacancies, He atoms or He–vacancy complexes to form coarse bubbles (Fig. 7(g)), which in turn can reduce the density of He bubbles.

Supplementary video related to this article can be found at https://doi.org/10.1016/j.jnucmat.2018.07.051.

5. Conclusions

In summary, the Ni/Gr with uniformly dispersive Gr was fabricated and the intrinsic disorder of Gr was introduced

simultaneously. Radiation tolerance was demonstrated by using 300 keV He^{2+} irradiation with a fluence of 1×10^{17} ions/cm^2 at 823 K. Pure Ni, which was used as reference material, was handled in the same condition. The analysis of Raman spectroscopy of Ni/Gr suggests that the intrinsic disorder of Gr mainly stems from its nanocrystallization and that the disorder of Gr can be further aggravated by elevated temperature and irradiation. As for the results of GIXRD and TEM, the radiation damage of the Ni matrix in Ni/Gr is not as significant as that of pure Ni. Less-disordered structures, such as lattice swelling and stacking faults, occur in Ni/Gr. Coarse He bubbles are more difficult to form in Ni/Gr than in pure Ni. The reason may be attributed to Gr's own capability in maintaining two-dimensional structure and inhibiting the formation of large-size defects. Thus, the stability of Ni/Gr interfaces is still able to be maintained by the disordered Gr, and the sink role of Ni/Gr interfaces is still present. With irradiation dose continuously increasing, high sp^3 amorphous carbon may rapidly arise in the Gr. In consideration of the higher operating temperatures of advanced fission reactors (*i.e.*, above 873 K), an intrinsic self-repair mechanism keeping the Gr in a crystalline state may be activated (Song et al. [65]). In addition, the crucial role of metal matrices for the healing of Gr defects has also been observed [71]. Consequently, even if irradiation induces considerable damage, the Gr may partly recover its intrinsic structure; this speculation suggests that the sink role of Ni/Gr interfaces may not completely disappear. All these results can provide reference for the service life assessment of metal−Gr composites in advanced fission reactors.

Acknowledgements

We thank Jinyu Li, Huiping Liu, Long Kang, and Tongmin Zhang for help during the ion irradiation experiments. The irradiation experimental work was performed on the 320 KV platform for multidiscipline research, with highly charged ions at the Institute of Modern Physics, CAS. We also appreciate Yuan Zhao, Adri C. T. van Duin and Rafael I. Gonzalez for help in preparing graphene oxide and the molecular dynamic simulations, respectively. This work was supported by the National Natural Science Foundation of China (Grant No. 11705087), the Natural Science Foundation of Jiangsu Province (Grant No. BK20170776), the Fundamental Research Funds for the Central Universities (Grant No. NJ20150021 & No. NT2018018), the Funding of Jiangsu Innovation Program for Graduate Education (Grant No. KYLX16_0350), and the Priority Academic Program Development of Jiangsu Higher Education Institutions.

Appendix A. Supplementary data

Supplementary data related to this article can be found at https://doi.org/10.1016/j.jnucmat.2018.07.051.

References

[1] J. Hwang, T. Yoon, S.H. Jin, J. Lee, T. Kim, S.H. Hong, et al., Enhanced mechanical properties of graphene/copper nanocomposites using a molecular−level mixing process, Adv. Mater. 25 (46) (2013) 6724−6729.
[2] Y. Kim, J. Lee, M.S. Yeom, J.W. Shin, H. Kim, Y. Cui, et al., Strengthening effect of single-atomic-layer graphene in metal−graphene nanolayered composites, Nat. Commun. 4 (2013) 2114.
[3] M. Han, P. Yuan, J. Liu, S. Si, X. Zhao, Y. Yue, et al., Interface energy coupling between β-tungsten nanofilm and few-layered graphene, Sci. Rep. 7 (1) (2017), 12213.
[4] X. Zhang, S. Si, X. Zhang, W. Wu, X. Xiao, C. Jiang, et al., Improved thermal stability of graphene-veiled noble metal nanoarrays as recyclable SERS substrates, ACS Appl. Mater. Interfaces 9 (46) (2017) 40726−40733.
[5] L.F. Dumée, L. He, Z. Wang, P. Sheath, J. Xiong, C. Feng, et al., Growth of nano-textured graphene coatings across highly porous stainless steel supports towards corrosion resistant coatings, Carbon 87 (2015) 395−408.
[6] X.M. Bai, A.F. Voter, R.G. Hoagland, M. Nastasi, B.P. Uberuaga, Efficient annealing of radiation damage near grain boundaries via interstitial emission, Science 327 (5973) (2010) 1631−1634.
[7] M.J. Demkowicz, A. Misra, A. Caro, The role of interface structure in controlling high helium concentrations, Curr Opin Solid St M 16 (3) (2012) 101−108.
[8] Y. Chen, K. Yu, Y. Liu, S. Shao, H. Wang, M.A. Kirk, et al., Damage-tolerant nanotwinned metals with nanovoids under radiation environments, Nat. Commun. 6 (2015) 7036.
[9] D. Chen, J. Wang, T. Chen, L. Shao, Defect annihilation at grain boundaries in alpha-Fe, Sci. Rep. 3 (2013) 1450.
[10] M.J. Demkowicz, R.G. Hoagland, J.P. Hirth, Interface structure and radiation damage resistance in Cu-Nb multilayer nanocomposites, Phys. Rev. Lett. 100 (13) (2008), 136102.
[11] Q. Wei, N. Li, N. Mara, M. Nastasi, A. Misra, Suppression of irradiation hardening in nanoscale V/Ag multilayers, Acta Mater. 59 (16) (2011) 6331−6340.
[12] W. Han, M.J. Demkowicz, N.A. Mara, E. Fu, S. Sinha, A.D. Rollett, et al., Design of radiation tolerant materials via interface engineering, Adv. Mater. 25 (48) (2013) 6975−6979.
[13] F. Chen, X. Tang, Y. Yang, H. Huang, D. Chen, Investigation of structural stability and magnetic properties of Fe/Ni multilayers irradiated by 300 keV Fe10+, J. Nucl. Mater. 452 (1−3) (2014) 31−36.
[14] T. Yang, L. Yang, H. Liu, H. Zhou, S. Peng, X. Zhou, et al., Ab initio study of stability and migration of point defects in copper-graphene layered composite, J. Alloy. Comp. 692 (2017) 49−58.
[15] H. Huang, X. Tang, F. Chen, Y. Yang, J. Liu, H. Li, et al., Radiation damage resistance and interface stability of copper−graphene nanolayered composite, J. Nucl. Mater. 460 (2015) 16−22.
[16] Y. Kim, J. Baek, S. Kim, S. Kim, S. Ryu, S. Jeon, et al., Radiation resistant vanadium-graphene nanolayered composite, Sci. Rep. 6 (2016) 24785.
[17] S. Si, W. Li, X. Zhao, M. Han, Y. Yue, W. Wu, et al., Significant radiation tolerance and moderate reduction in thermal transport of a tungsten nanofilm by inserting monolayer graphene, Adv. Mater. 29 (2017) 1604623.
[18] R.I. González, F. Valencia, J. Mella, A.C.T. van Duin, K.P. So, J. Li, et al., Metal-nanotube composites as radiation resistant materials, Appl. Phys. Lett. (2016) 109, 033108.
[19] R.W. Grimes, R.J.M. Konings, L. Edwards, Greater tolerance for nuclear materials, Nat. Mater. 7 (9) (2008), 683.
[20] S.J. Zinkle, G.S. Was, Materials challenges in nuclear energy, Acta Mater. 61 (3) (2013) 735−758.
[21] K.L. Murty, I. Charit, Structural materials for Gen-IV nuclear reactors: challenges and opportunities, J. Nucl. Mater. 383 (1−2) (2008) 189−195.
[22] C. Lu, L. Niu, N. Chen, K. Jin, T. Yang, P. Xiu, et al., Enhancing radiation tolerance by controlling defect mobility and migration pathways in multicomponent single-phase alloys, Nat. Commun. 7 (2016) 13564.
[23] M. Samaras, M. Victoria, Modelling in nuclear energy environments, Mater. Today 11 (12) (2008) 54−62.
[24] G.R. Odette, M.J. Alinger, B.D. Wirth, Recent developments in irradiation-resistant steels, Annu. Rev. Mater. Res. 38 (2008) 471−503.
[25] P. Yvon, F. Carré, Structural materials challenges for advanced reactor systems, J. Nucl. Mater. 385 (2) (2009) 217−222.
[26] R.E. Stoller, Molecular dynamics simulation of cascade-induced ballistic helium resolutioning from bubbles in iron, J. Nucl. Mater. 442 (1−3) (2013) S674−S679.
[27] C. Lu, Z. Lu, R. Xie, C. Liu, L. Wang, Microstructure of HIPed and SPSed 9Cr-ODS steel and its effect on helium bubble formation, J. Nucl. Mater. 474 (2016) 65−75.
[28] F. Gao, H. Heinisch, R.J. Kurtz, Diffusion of He interstitials in grain boundaries in α-Fe, J. Nucl. Mater. 351 (1−3) (2006) 133−140.
[29] M. Saleh, Z. Zaidi, M. Lonescu, C. Hurt, K. Short, J. Daniels, et al., Relationship between damage and hardness profiles in ion irradiated SS316 using nanoindentation−experiments and modelling, Int. J. Plast. 86 (2016) 151−169.
[30] G.J. Galloway, G.J. Ackland, Molecular Dynamics and object kinetic Monte Carlo study of radiation-induced motion of voids and He bubbles in Bcc iron, Phys. Rev. B 87 (10) (2013), 104106.
[31] X. Zhang, N. Li, O. Anderoglu, H. Wang, J.G. Swadener, T. Höchbauer, et al., Nanostructured Cu/Nb multilayers subjected to helium ion-irradiation, Nucl. Instrum. Meth. B 261 (1−2) (2007) 1129−1132.
[32] Z. Dai, X. Xiao, W. Wu, Y. Zhang, L. Liao, S. Guo, et al., Plasmon-driven reaction controlled by the number of graphene layers and localized surface plasmon distribution during optical excitation, Light Sci. Appl. 4 (10) (2015) e342.
[33] S. Pei, H.M. Cheng, The reduction of graphene oxide, Carbon 50 (9) (2012) 3210−3228.
[34] M. Lorenzoni, A. Giugni, E.D. Fabrizio, F. Pérez-Murano, A. Mescola, B. Torre, Nanoscale reduction of graphene oxide thin films and its characterization, Nanotechnology 26 (28) (2015), 285301.
[35] Z. Hu, G. Tong, D. Lin, C. Chen, H. Guo, J. Xu, et al., Graphene-reinforced metal matrix nanocomposites−A review, Mater. Sci. Technol. 32 (9) (2016) 930−953.
[36] H.G.P. Kumar, M.A. Xavior, Graphene reinforced metal matrix composite (GRMMC): a review, Procedia Engineering 97 (2014) 1033−1040.
[37] C. Gómez-Navarro, J.C. Meyer, R.S. Sundaram, A. Chuvilin, S. Kurasch, M. Burghard, et al., Atomic structure of reduced graphene oxide, Nano Lett. 10 (4) (2010) 1144−1148.
[38] C. Botas, P. Álvarez, C. Blanco, M.D. Gutiérrez, P. Ares, R. Zamani, et al., Tailored

graphene materials by chemical reduction of graphene oxides of different atomic structure, RSC Adv. 2 (25) (2012) 9643–9650.
[39] M.K. Rabchinskii, V.V. Shnitov, A.T. Dideikin, A.E. Aleksenskii, S.P. Vul, M.V. Baidakova, et al., Nanoscale perforation of graphene oxide during photoreduction process in the argon atmosphere, J. Phys. Chem. C 120 (49) (2016) 28261–28269.
[40] C.L.P. Pavithra, B.V. Sarada, K.V. Rajulapati, T.N. Rao, G. Sundararajan, A new electrochemical approach for the synthesis of copper-graphene nanocomposite foils with high hardness, Sci. Rep. 4 (2014) 4049.
[41] G. Compagnini, F. Giannazzo, S. Sonde, V. Raineri, E. Rimini, Ion irradiation and defect formation in single layer graphene, Carbon 47 (14) (2009) 3201–3207.
[42] J. Kotakoski, A.V. Krasheninnikov, U. Kaiser, J.C. Meyer, From point defects in graphene to two-dimensional amorphous carbon, Phys. Rev. Lett. 106 (10) (2011), 105505.
[43] O. Lehtinen, J. Kotakoski, A.V. Krasheninnikov, A. Tolvanen, K. Nordlund, J. Keinonen, Effects of ion bombardment on a two-dimensional target: atomistic simulations of graphene irradiation, Phys. Rev. B 81 (15) (2010), 153401.
[44] E.H. Åhlgren, S.K. Hämäläinen, O. Lehtinen, P. Liljeroth, J. Kotakoski, Structural manipulation of the graphene/metal interface with Ar+ irradiation, Phys. Rev. B 88 (15) (2013), 155419.
[45] Z. Bai, L. Zhang, H. Li, L. Liu, Nanopore creation in graphene by ion beam irradiation: geometry, quality, and efficiency, ACS Appl. Mater. Interfaces 8 (37) (2016) 24803–24809.
[46] H. Huang, X. Tang, F. Chen, J. Liu, H. Li, D. Chen, Graphene damage effects on radiation-resistance and configuration of copper–graphene nanocomposite under irradiation: a molecular dynamics study, Sci. Rep. 6 (2016) 39391.
[47] H. Huang, W. Zhang, M.D.L. Reyes, X. Zhou, C. Yang, R. Xie, et al., Mitigation of He embrittlement and swelling in nickel by dispersed SiC nanoparticles, Mater. Des. 90 (2016) 359–363.
[48] S. Jin, X. He, T. Li, S. Ma, R. Tang, L. Guo, Microstructural evolution in nickel alloy C-276 after Ar-ion irradiation at elevated temperature, Mater. Char. 72 (2012) 8–14.
[49] ASTM Standard E521–96, Standard practice for neutron radiation damage simulation by charged-particle irradiation, American Society for Testing and Materials Intl., 2009.
[50] Y. Zhao, C. Zhang, T. Liu, R. Fan, H. Tao, J. Xue, Low temperature green synthesis of sulfur-nitrogen co-doped graphene as efficient metal-free catalysts for oxygen reduction reaction, Int J Electrochem Sci 12 (4) (2017) 3537–3548.
[51] D. Kuang, L. Xu, L. Liu, W. Hu, Y. Wu, Graphene–nickel composites, Appl. Surf. Sci. 273 (2013) 484–490.
[52] A. Ganguly, S. Sharma, P. Papakonstantinou, J. Hamilton, Probing the thermal deoxygenation of graphene oxide using high-resolution in situ X-ray-based spectroscopies, J. Phys. Chem. C 115 (34) (2011) 17009–17019.
[53] J.F. Ziegler, M.D. Ziegler, J.P. Biersack, SRIM–The stopping and range of ions in matter (2010), Nucl. Instrum. Meth. B 268 (11–12) (2010) 1818–1823.
[54] M.S. Seehra, V. Narang, U.K. Geddam, A.B. Stefaniak, Correlation between X-ray diffraction and Raman spectra of 16 commercial graphene–based materials and their resulting classification, Carbon 111 (2017) 380–385.
[55] A.C. Ferrari, D.M. Basko, Raman spectroscopy as a versatile tool for studying the properties of graphene, Nat. Nanotechnol. 8 (4) (2013) 235–246.
[56] S. Plimpton, Fast parallel algorithms for short-range molecular dynamics, J. Comput. Phys. 117 (1) (1995) 1–19.
[57] A.C.T. van Duin, S. Dasgupta, F. Lorant, W.A. Goddard, ReaxFF: a reactive force field for hydrocarbons, J. Phys. Chem. 105 (41) (2001) 9396–9409.
[58] A. Stukowski, Visualization and analysis of atomistic simulation data with OVITO–the Open Visualization Tool, Model Simul Mater Sc 18 (1) (2009), 015012.
[59] L.G. Cançado, M.G. da Silva, E.H.M. Ferreira, F. Hof, K. Kampioti, K. Huang, et al., Disentangling contributions of point and line defects in the Raman spectra of graphene-related materials, 2D Mater. 4 (2) (2017), 025039.
[60] L.M. Malard, M.A. Pimenta, G. Dresselhaus, M.S. Dresselhaus, Raman spectroscopy in graphene, Phys. Rep. 473 (5–6) (2009) 51–87.
[61] A.K. Srivastav, N. Chawake, B.S. Murty, Grain-size-dependent non-monotonic lattice parameter variation in nanocrystalline W: the role of non-equilibrium grain boundary structure, Scripta Mater. 98 (2015) 20–23.
[62] D. Ali, M.Z. Butt, Structural characteristics and inverse Hall–Petch relation in high-purity nickel irradiated with nanosecond infrared laser pulses, Physica B 444 (2014) 77–84.
[63] B.E. Warren, X-ray Diffraction, Dover Publications Inc, New York, 1969.
[64] A.C. Ferrari, J. Robertson, Interpretation of Raman spectra of disordered and amorphous carbon, Phys. Rev. B 61 (20) (2000), 14095.
[65] B. Song, G.F. Schneider, Q. Xu, G. Pandraud, C. Dekker, H. Zandbergen, Atomic-scale electron-beam sculpting of near-defect-free graphene nanostructures, Nano Lett. 11 (6) (2011) 2247–2250.
[66] M.A. Pimenta, G. Dresselhaus, M.S. Dresselhaus, L.G. Cançado, A. Jorio, R. Saito, Studying disorder in graphite-based systems by Raman spectroscopy, Phys. Chem. Chem. Phys. 9 (11) (2007) 1276–1290.
[67] L.G. Cançado, A. Jorio, E.H.M. Ferreira, F. Stavale, C.A. Achete, R.B. Capaz, et al., Quantifying defects in graphene via Raman spectroscopy at different excitation energies, Nano Lett. 11 (8) (2011) 3190–3196.
[68] B. Wang, Y. Puzyrev, S.T. Pantelides, Strain enhanced defect reactivity at grain boundaries in polycrystalline graphene, Carbon 49 (12) (2011) 3983–3988.
[69] L. Adamska, Y. Lin, A.J. Ross, M. Batzill, Oleynik II, Atomic and electronic structure of simple metal/graphene and complex metal/graphene/metal interfaces, Phys. Rev. B 85 (19) (2012), 195443.
[70] H. Huang, X. Tang, F. Chen, F. Gao, Q. Peng, L. Ji, et al., Self-healing mechanism of irradiation defects in nickel–graphene nanocomposite: an energetic and kinetic perspective, J. Alloy. Comp. 765 (2018) 253–263.
[71] P. Jacobson, B. Stöger, A. Garhofer, G.S. Parkinson, M. Schmid, R. Caudillo, et al., Disorder and defect healing in graphene on Ni (111), J. Phys. Chem. Lett. 3 (1) (2011) 136–139.